Carbohydrate Polymers 356 (2025) 123399

Contents lists available at ScienceDirect

Carbohydrate Polymers

journal homepage: www.elsevier.com/locate/carbpol

Kinetics and selectivity insights into carbon dioxide capture utilizing carboxymethyl cellulose-polypyrrole nanocomposites: Screening of silane functionalization

Mohammed G. Kotp [a], Islam M. Minisy [b], Basel Al-Saida [c], Shiao-Wei Kuo [a,d,*]

[a] Department of Materials and Optoelectronic Science, National Sun Yat-Sen University, Kaohsiung 80424, Taiwan
[b] Institute of Macromolecular Chemistry, Czech Academy of Sciences, 16200 Prague, Czech Republic
[c] Department of Chemistry, Faculty of Science, Al-Balqa Applied University, Salt 19117, Jordan
[d] Department of Medicinal and Applied Chemistry, Kaohsiung Medical University, Kaohsiung 807, Taiwan

ARTICLE INFO

Keywords:
Carboxymethyl cellulose (CMC)
Polypyrrole
Nanocomposites
CO_2 capture
Silane functionalization

ABSTRACT

Cellulose is a highly versatile and abundant biopolymer that holds significant promise for enhancing capture technologies due to its inherent properties. However, to maximize its effectiveness in carbon dioxide (CO_2) adsorption, it is essential to enhance its properties through chemical or physical modifications. By developing cellulose-based materials with tailored functionalities, we can create sustainable sorbents that not only contribute to reducing greenhouse gas emissions but also leverage low-cost and environmentally friendly resources, making them suitable for large-scale applications in carbon capture technologies. This study demonstrates the synthesis of carboxymethyl cellulose-polypyrrole (CMC-PP) nanocomposite and its coating with (3-aminopropyl)triethoxysilane (APTS) or (3-mercaptopropyl)trimethoxysilane (MPTS) to derive CMC-PP-NH_2 and CMC-PP-SH nanocomposites, respectively. The designed composites' physicochemical properties were studied using various analytical techniques. The CO_2 and N_2 capture capabilities of CMC-PP, CMC-PP-NH_2, and CMC-PP-SH nanocomposites were investigated. Among them, the CMC-PP-SH nanocomposite has exhibited the highest CO_2 adsorption capacity of 49.6 cm^3g^{-1}. Adsorption isotherms fitting using the dual-site Langmuir model and calculation of standard enthalpy changes (Q_{st}) reveal that the thiol groups in CMC-PP-SH provide the most favourable interactions for CO_2 capture. These findings demonstrate the potential utilization of silane coatings to develop advanced materials for effective gas adsorption and separation technologies.

1. Introduction

Carbon dioxide (CO_2) emissions from human activities have reached record levels, contributing significantly to climate change and global warming (Barsoum et al., 2024; Boubaker et al., 2024; Kotp & Kuo, 2024). To mitigate these environmental concerns, various carbon capture technologies have been developed, including post-combustion, pre-combustion, and oxy-fuel combustion processes (Chao et al., 2021). Among these, post-combustion capture is the most mature and widely used method, although it faces challenges such as high energy requirements and additional costs (Mohamed et al., 2022; Mousa et al., 2023).

Biopolymers, particularly carboxymethyl cellulose (CMC), have gained attention in CO_2 capture applications due to their renewable nature, biodegradability, and ability to interact with various materials (Venturi et al., 2019; Wu et al., 2024). Realistically, CMC was preferred over cellulose nanofiber due to its superior water solubility, functional versatility, cost-effectiveness and excellent film-forming properties (Kawasaki et al., 2016; Rahman et al., 2021). However, the adsorption performance of pristine CMC is often limited (3.47 cm^3g^{-1}) necessitating the development of nanocomposites by combining it with synthetic polymers like polypyrrole (PP) (Adhikari et al., 2018; Kotp, Torad, Nara, et al., 2023). CMC is an anionic polymer that can form hydrogen bonds and interact electrostatically with PP (Tanzifi et al., 2020). On the other hand, PP is a conducting polymer known for its electrical conductivity and environmental stability. Such a combination of CMC and PP can enhance the environmental stability and adsorption capacity (Chen et al., 2023; Minisy et al., 2024).

* Corresponding author at: Department of Materials and Optoelectronic Science, National Sun Yat-Sen University, Kaohsiung 80424, Taiwan.
E-mail address: kuosw@faculty.nsysu.edu.tw (S.-W. Kuo).

https://doi.org/10.1016/j.carbpol.2025.123399
Received 18 September 2024; Received in revised form 16 January 2025; Accepted 13 February 2025
Available online 16 February 2025

One of the main challenges in developing effective nanocomposites for CO_2 capture is ensuring strong interactions between the biopolymer and those manmade ones (Banerjee et al., 2023; Seidi et al., 2022). To address this issue, researchers have explored coating the derived nanocomposites with silane sources, such as (3-aminopropyl)trimethoxysilane (APTS) (Fatima et al., 2021). Herein, our study hypothesizes that the incorporation of PP into CMC-based nanocomposites significantly enhances their CO_2 adsorption capacity due to the synergistic effects of the structural porosity of CMC and the reactive properties of PP. Moreover, APTS and (3-mercaptopropyl)trimethoxysilane (MPTS) were used to coat CMC-PP to obtain new functionalized nanocomposite denoted as CMC-PP-NH_2, and CMC-PP-SH, respectively. Such functionalization of CMC-PP can motivate the physio and chemical interactions between the CMC-PP nanocomposites and CO_2 molecules (Shishatskiy et al., 2010). This novel approach is expected to enhance CO_2 capture by developing dual-functionality CMC-PP nanocomposites through improved surface chemistry. The dual approach of the in-situ polymerization of pyrrole onto CMC followed by silane modification allows us to leverage the unique benefits of both processes, resulting in a more effective sorbent for CO_2 capture.

In this study, CMC-PP, CMC-PP-NH_2, and CMC-PP-SH (Scheme 1) were prepared, and thorough molecular and physical characterizations were used to clarify their remarkable properties. In the meantime, their CO_2 and N_2 capture capabilities were investigated. The adsorption isotherms of Langmuir, dual-site Langmuir (DSL), and Sips models were fitted to study these materials' adsorption mechanisms and efficiencies. Additionally, the standard enthalpy changes (isosteric heat of sorption, Q_{st}) using the Clausius-Clapeyron equation to understand the energetics of the adsorption process. The findings contribute to the development of advanced materials for effective CO_2 capture technologies, addressing the pressing need for sustainable solutions to mitigate climate change.

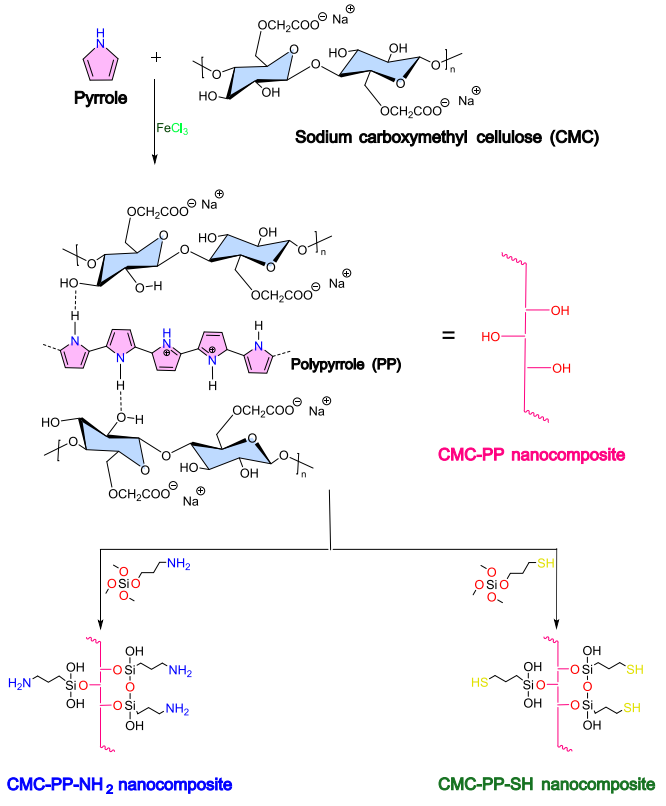

Scheme 1. Synthesis sketch of CMC-PP, CMC-PP-NH_2, and CMC-PP-SH nanocomposites.

2. Materials and methods

2.1. Materials

In the experimental procedures outlined in this research, a variety of chemicals were utilized. Sodium carboxymethyl cellulose (CMC) of medium viscosity, with a purity of 99 % and a degree of substitution (DS) ranging from 0.6 to 0.95, (average Mw ~ 90,000) were obtained from Showa Chemicals (Japan). Pyrrole sourced from TCI America (USA). The iron(III) chloride ($FeCl_3$) used in the experiments was obtained from Acros Organics (USA). Additionally, (3-aminopropyl)trimethoxysilane (APTS, 98 %) and (3-mercaptopropyl)trimethoxysilane (MPTS, 98 %) were acquired from Sigma Aldrich. The hydrochloric acid solution (HCl, 35 %) employed originated from Showa Chemicals, while toluene was sourced from Alfa Aesar Chemicals. All materials utilized in the study were used in their as-received state.

2.2. Synthesis of CMC-PP nanocomposite

In a controlled laboratory setting, the nanocomposite of CMC and PP was prepared using a meticulous in-situ methodology. Initially, 0.5 g of CMC was dissolved in 50 mL of water within an ice bath environment. The solution was stirred at a consistent rate of 450 rpm for 45 min. Subsequently, 10 mL of hydrochloric acid (1 M) was introduced, followed by the addition of 0.25 mL of pyrrole. The resulting mixture was left to stir for an additional 3 h. Following this, the mixture underwent further stirring for 2 h and was pre-cooled before the gradual addition of 1.41 g of $FeCl_3$. The composite was then left to stir continuously for 24 h. Finally, the nanocomposite of CMC-PP in its doped form was collected by centrifugation. The CMC-PP nanocomposite was carefully dried in an oven under ambient air atmosphere at 80 °C to obtain powder form (Fig. S1).

2.3. Synthesis of CMC-PP-NH_2 nanocomposite

Following the preparation of the CMC-PP nanocomposite, a post-grafting method was employed to coat the nanocomposite with APTS, resulting in the formation of CMC-PP-NH_2. Initially, 0.5 g of the CMC-PP nanocomposite was combined with 1 mL of APTS. This mixture was then introduced into a 20 mL dry toluene environment and subjected to reflux for 10 h to facilitate the coating process. Subsequently, the mixture underwent washing using methylene chloride for a duration of 24 h to remove any unreacted components and impurities. The obtained sample was carefully dried in an oven under ambient air atmosphere at 80 °C conditions for 24 h to ensure complete removal of solvents and moisture of the produced powder. Notably, the digital images of the utilized polymers and nanocomposites are provided in the Supporting Information file Fig. S1.

2.4. Synthesis of CMC-PP-SH nanocomposite

A post-grafting method was utilized to coat the CMC-PP nanocomposite with MPTS, leading to the creation of a novel functionalized nanocomposite identified as CMC-PP-SH. This process involved the thorough mixing of 1.5 g of CMC-PP and dry toluene (25 mL), followed by reflux and magnetic stirring under N_2 for 1 h. Subsequently, 1.5 mL of 3-MPTS was charged into the mixture and then refluxed for an extra two days. After allowing the product to settle for 3 h, CMC-PP-SH nanocomposite powder (Fig. S1) was extracted, rinsed with ethanol, and ultimately dried at 80 °C for 24 h.

Notably, during the in-situ polymerization process to form the CMC-PP nanocomposite, the hydroxyl groups are likely to remain intact on the surface of the CMC backbone, even after the polymerization of pyrrole. The retained hydroxyl groups on the CMC-PP nanocomposite provide active sites for further functionalization. Moreover, the interactions between PP of the CMC-PP and APTS, MPTS compounds

primarily involve hydrophobic interactions, rather than traditional covalent bonding mechanisms. Both APTS and MPTS possess hydrophobic segments due to their alkyl chains. These hydrophobic interactions can facilitate compatibility between the hydrophobic PP surface and the silane coatings, further enhancing adhesion.

2.5. Characterizations

Contemporary KBr discs were utilized for FTIR runs using a 27 Bruker Tensor analyzer. The precision levels were set to 4 cm^{-1}. Thermogravimetric analysis (TGA) of CMC-PP, CMC-PP-NH_2, and CMC-PP-SH nanocomposite were carried out over N_2 fluid utilizing the TA Q-50 apparatus. A locked Pt cane was utilized as the specimen container, afterwards the ambient temperature was pushed up to 800 °C with a gradient of 20 °C min^{-1} and a median N_2 stream of 60 mL min^{-1}. Micromeritics ASAP 2020 surface area and porosity analyzers were utilized to evaluate the surface area along with the porosity of CMC-PP, CMC-PP-NH_2, and CMC-PP-SH nanocomposite. The use of an ultrapure N_2 flow (up to around 1 atm) and a liquefied N_2 immersion enabled the acquisition of nitrogenic isotherms much easier. Thermo Fisher Scientific ESCALAB 250 utilized a tiny monochromatic Al Kα X-ray laser (15 kV) and a dual-focusing entire 180 spheric sectoral electron scanner to conduct XPS investigations. The JEOL JSM-7610F SEM was utilized to visualize FE-SEM information. CMC-PP, CMC-PP-NH_2, and CMC-PP-SH nanocomposites got sputtered with Pt lasting 150 s to ensure explicit vision. Upon demonstrating the CMC-PP, CMC-PP-NH_2, and CMC-PP-SH nanocomposites to 200 KV, TEM representations were performed using a JEOL-2100 electron microscope.

2.6. Solubility

From a chemical stability perspective, the CMC nanocomposites exhibited insolubility in organic solvents such as methanol, ethanol, dioxane, chloroform, and tetrahydrofuran, as well as in acidic and alkaline solutions. This indicates a high level of cross-linking and exceptional chemical stability. Therefore, we anticipated that our CMC nanocomposites would preserve their morphologies and chemical structures after washing or exposure to acidic or alkaline solutions, performing better in this regard compared to other reported polymers (Ahmed et al., 2022; Kotp et al., 2021).

2.7. Acquiring isotherms

Utilizing a gas absorbing analyzer (ASAP 2020; Micromeritics), both CO_2 and N_2 intake isotherms of CMC-PP, CMC-PP-NH_2, and CMC-PP-SH nanocomposites at 298 and 273 K have been determined. Generally, the given samples (between 30 and 90 mg) were evacuated and dried at 100 °C for five hours. Subsequently, the samples were put into analyzer tubes in order to measure the gas-uptake isotherms at 298 K and 273 K by gradually injecting either highly pure CO_2 or N_2 fluids (up to approximately 1 atm). We used CO_2 and N_2 sorption levels at high verified levels (P/P_0) of 1 for a comparison assessment.

2.8. Selectivity assays

The theory of Henry's law was implemented to estimate the selectivity assessment of CMC-PP, CMC-PP-NH_2, and CMC-PP-SH nanocomposites between CO_2/N_2, as earlier explained. Interestingly, at 0.1 bar of pressure reduction, the Henry's law constant takes into account the slope of the single-component gas uptake loop.

2.9. Reusability assays

The reusability of the CMC-PP-NH_2 and CMC-PP-SH nanocomposites was evaluated through a series of adsorption-desorption cycles conducted at two different temperatures of 273 K and 298 K. Firstly, a known mass of each nanocomposite powder was placed in a testing BET tube, and CO_2 was introduced to allow for adsorption at the specified temperature. The system was maintained at either 273 K or 298 K during the adsorption to ensure consistent conditions. Firstly, the composite was degassed at 403 K to remove any residual gases or moisture, then the sample is cooled to the desired adsorption temperature in the analysis port. After reaching equilibrium, CO_2 desorption was performed in a nitrogen atmosphere at 403 K. This step is critical to prepare the nanocomposite for the next adsorption cycle. This protocol was repeated for five adsorption-desorption cycles to assess the stability and reusability of our composites as reported previously (Deng et al., 2012; Ouyang et al., 2018). The amount of CO_2 adsorbed during each cycle was recorded to assess the adsorption capacity.

3. Results and discussion

The crosslinking of CMC with PP occurs primarily through hydrogen bonding between the CMC hydroxyl groups and the amino groups of PP. The silane modification further enhances this interaction by providing additional reactive sites and improving the overall functionality of the nanocomposite. The tailored properties of CMC-PP nanocomposites, driven by functionalization with APTS and MPTS, not only enhance their structural integrity but also optimize their performance as effective adsorbents for CO_2 capture. This highlights the potential of these materials in developing advanced solutions for carbon capture technologies.

3.1. FTIR spectroscopy

The FTIR spectroscopy (Fig. 1) revealed distinct peaks corresponding to the functional groups in pristine CMC and CMC-PP composite, and its functionalized forms with APTS and MPTS.

Pristine CMC displays featured signals at 3440 cm^{-1} (O—H stretching of CMC and adsorbed water molecules), 2910 cm^{-1} (C—H stretching), 1611 cm^{-1} (–COO^-), 1429 cm^{-1} (C—H bending), and 1062 cm^{-1} (C—O stretching), elucidating the hydroxyl groups, aliphatic components, carbonyl groups, ether linkages, and methyl/methylene groups, respectively (Habibi, 2014). The FTIR spectrum of the CMC-PP nanocomposite aligned well with the characteristic functional groups present in both CMC and PP (Fig. 1). Compared to pristine CMC, the CMC-PP nanocomposite showed a slight shift in the O—H stretching peak (3408 cm^{-1}), indicating potential hydrogen bonding interactions between the components (Tanzifi et al., 2020). Additionally, the new peaks observed at 1544 cm^{-1} (CC pyrrole ring stretching), 1453 cm^{-1} (C—C) and 964 cm^{-1} (=C–H out-of-plane deformation), confirming the successful incorporation of PP into the CMC matrix (Kumar et al., 2022; Minisy et al., 2021). The shifted and altered peak intensities compared to pristine CMC suggested chemical modifications and interactions that occurred during composite formation.

Functionalization of the CMC-PP nanocomposite with APTS and MPTS was further investigated using FTIR spectroscopy (Fig. 1). The APTS-functionalized nanocomposite displayed a new band at 1036 cm^{-1}, attributed to Si–O–Si stretching vibrations from APTS coating, along with characteristic peaks corresponding to CMC and PP (Prodan et al., 2021). In the case of CMC-PP-SH nanocomposite, –SH peaks are not clearly visible in the spectra due to the strong stretching vibration of Si—O at 1057 cm^{-1}. These observations confirmed the successful functionalization of the CMC-PP nanocomposite with APTS and MPTS.

3.2. XPS

XPS analysis was employed to investigate the elemental composition and chemical state of the CMC-PP composite and its functionalized forms with APTS and MPTS. The XPS analysis (Fig. S2) confirmed the presence of expected elements, including carbon (C1s), oxygen (O1s), and nitrogen (N1s), in all samples, consistent with the composition of

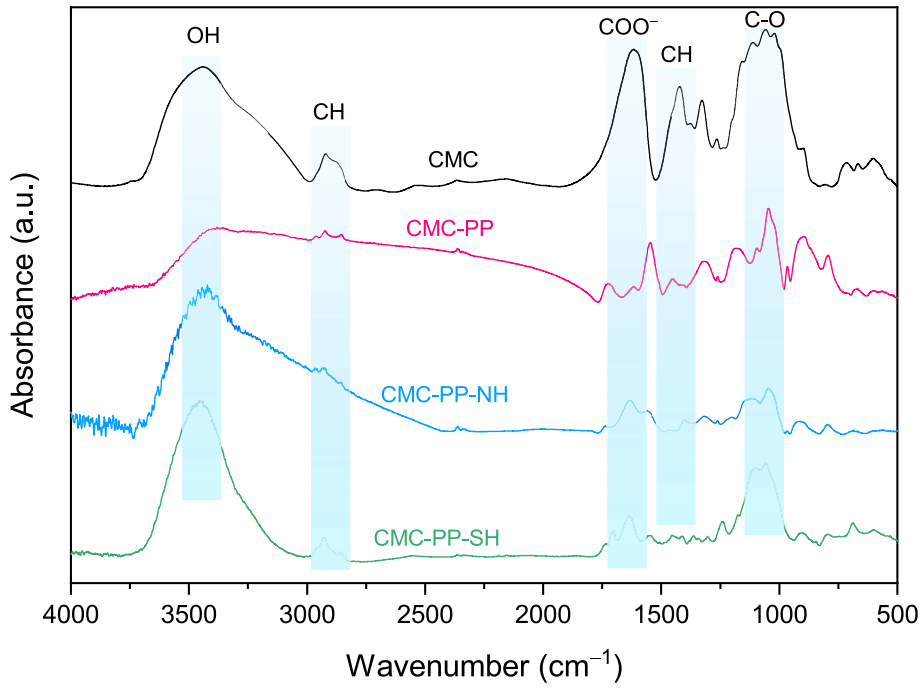

Fig. 1. FTIR spectra of CMC, CMC-PP, CMC-PP-NH_2, and CMC-PP-SH composites.

CMC-PP, CMC-PP-NH_2, and CMC-PP-SH composites. Interestingly, an additional S2p peak was detected in the XPS spectrum of the CMC-PP-SH (Fig. 2d) confirming the successful incorporation of sulfur-containing units from the MPTS shell onto the CMC-PP composite surface. The high-resolution XPS data provided for the deconvolution of the C1s peaks of CMC-PP, CMC-PP-NH_2, and CMC-PP-SH reveals the presence of different carbon states (Fig. 2). The peaks observed at 283.6, 284.2, 285, and 287 eV correspond to C═C, C═N, C-OH, and C═O & C—Si, respectively (Fig. 2a). As provided in Table S1, the areas under these peaks indicate the relative abundance of these functional groups in the samples. One can notice the increment in the C—N peak within the CMC-PP-NH_2 nanocomposite attributed to the inclusion of the APTS (Table S1). Due to the close binding energies of those C—O, C—S, and C–S–H units, the C1s state at 285 eV cannot be utilized to discriminate among them precisely (Kotp, Kuo, & EL-Mahdy, 2024; Kotp, Torad, Nara, et al., 2023). However, we can observe an increment of this band

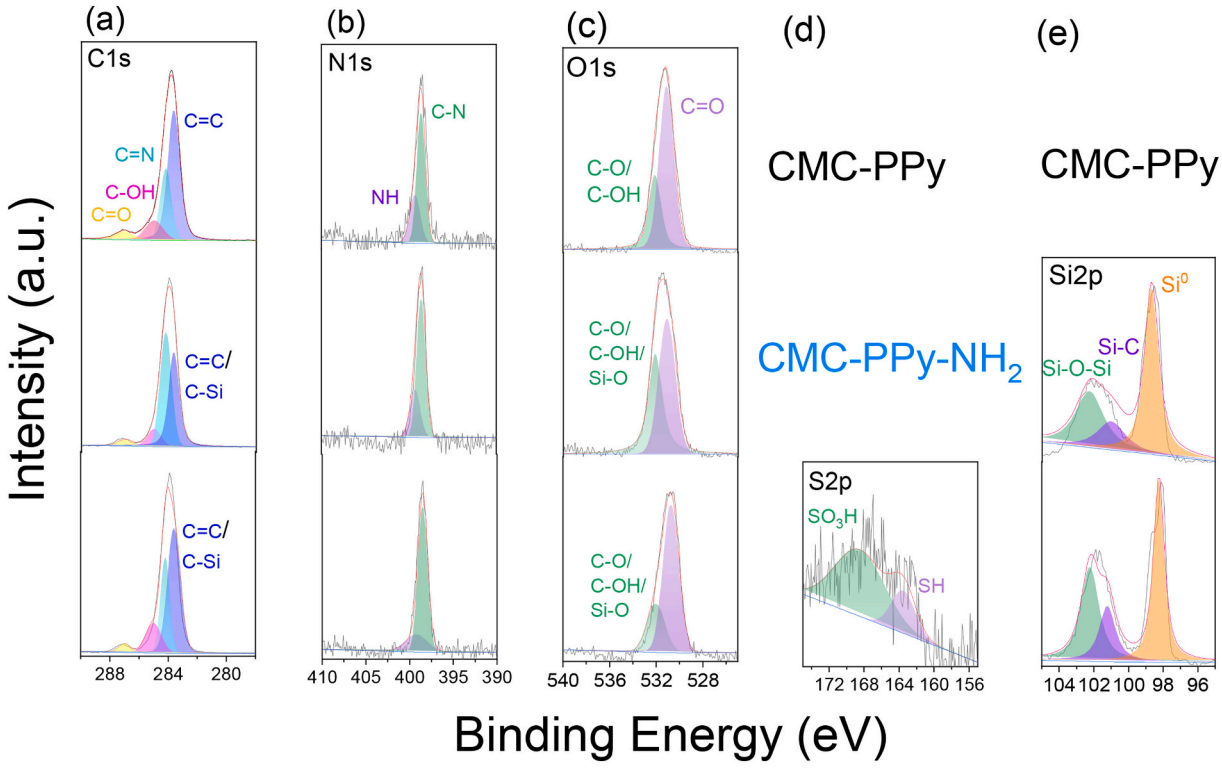

Fig. 2. HRXPS scan of C1s, N1s, O1s, S2p, and Si2p incorporated those CMC-PP, CMC-PP-NH_2, and CMC-PP-SH nanocomposites.

in the CMC-PP-SH nanocomposite exhibiting a considerable amount of thiol groups. These results indicate the varying composition of carbon functional groups in the different samples, providing valuable insights into the surface chemistry and modifications achieved through the coating processes.

The deconvolution of N1s spectra of CMC composites implies the existence of a couple of nitrogen states at 398.6 and 399.1 eV detectable to pyrrolic-N and N—H, respectively (Fig. 2b) (Hsiao et al., 2024). Importantly, the N species from PP and APTS compounds appear at similar binding energies at 399.1 complicating differentiation between them, thus the overlap between their binding energies makes it difficult to assign specific contributions to either PP or APTS definitively. On the other hand, the CMC-PP-NH_2 nanocomposite reveals a high percentage of N—H units (Table S1) again confirming the presence of the APTS, and potentially indicating enhanced interactions or modifications on the surface of the materials. These results indicate variations in the composition of nitrogen-containing functional groups in the composites.

The O1s peaks of CMC-PP, CMC-PP-NH_2, and CMC-PP-SH nanocomposites revealing two distinct peaks corresponding to C–O/C–OH and C═O at 532.09 and 531.09 eV, respectively (Fig. 2c) (Kotp, Torad, Lüder, et al., 2023). The deconvolution of the S2p peak in the XPS spectrum of CMC-PP-SH reveals the presence of S2p species in different chemical states. Specifically, the peaks observed at 168.5 eV correspond to SO_3H (sulfonic acid groups), while those at 163.5 eV indicate S—H (sulfhydryl groups) (Fig. 2d). An oxidation might account for the CMC-PP-SH nanocomposite surface, as a result of exposure to oxygen and moisture as well. The identification of SO_3H and S—H functionalities is significant in understanding the surface chemistry and functionalization of the material. Importantly, XPS analysis of the Si-incorporated CMC-PP-NH_2 and CMC-PP-SH nanocomposites revealed the presence of Si-O-Si, Si—C, and Si^0 bonds at binding energies of 102.25 eV, 100.91 eV, and 98.73 eV, respectively (Fig. 2e). The Si^0 signal may be attributed to the silicon wafers used as substrates during the XPS analysis. This observation suggests that silane functionalization is successful.

3.3. BET specific surface area and porosity

The BET surface area measurements of the CMC-PP, CMC-PP-NH_2 and CMC-PP-SH nanocomposites provide crucial insights into the available surface area for their interactions. Fig. 3a reveals that the adsorption isotherm observed for the CMC-PP nanocomposite is a type IV isotherm (IUPAC classification) with a hysteresis loop. This indicates a multilayer physical adsorption of mesoporous structures (Kumar et al., 2021). The BET surface areas of 10.35 and 4.49 m^2g^{-1} were achieved for CMC-PP, and CMC-PP-NH_2 nanocomposite, respectively (Fig. 3a). Otherwise, the CMC-PP-SH nanocomposite demonstrated the highest BET surface area, albeit modest, of 32.85 m^2g^{-1}. The substantial increase by 3 times in the BET surface area of the CMC-PP nanocomposite after coating with MPTS suggests a notable enhancement in surface properties, potentially leading to improved performance compared to the pristine CMC-PP and the CMC-PP-NH_2 nanocomposite.

The BJH (Barrett-Joyner-Halenda) method was applied to calculate the pore diameter, volume, and distribution based on capillary condensation principles (Yang & Wang, 2024). The porosity observed in the nanocomposite (Fig. 3b) can be attributed to the templating effect of CMC during polymerization, which creates voids within the material, ultimately leading to the development of a porous structure (Mudassir et al., 2021; Qiu & Netravali, 2014). The measured pore widths of the CMC-PP, CMC-PP-NH_2 and CMC-PP-SH nanocomposites were found to vary among the different samples. Specifically, the CMC-PP shows pore widths of 8.61 nm and 12.81 nm, the CMC-PP-NH_2 nanocomposite shows pore widths of 7.38 nm and 11.38 nm, while the CMC-PP-SH nanocomposite displays pore widths of 3.75 nm, 5.47 nm, 9.57 nm, and 18.72 nm. The decrease in pore width observed in the CMC-PP-NH_2 and CMC-PP-SH nanocomposites indicates a potential densification or pore-sealing effect caused by the coating process (Rapheal et al., 2016). However, in the case of CMC-PP-SH nanocomposite, new wider pores have been created during the functionalization process. These results suggest that the surface modifications with APTS and MPTS have influenced the pore structure of the CMC-PP nanocomposite.

3.4. Thermal gravimetric analysis

The pristine CMC, CMC-PP, CMC-PP-NH_2, and CMC-PP-SH nanocomposites TGA revealed significant differences in char yield and thermal degradation temperatures (Fig. S3). The char yield increased progressively from the pristine CMC to the CMC-PP nanocomposite, further enhanced in the CMC-PP-NH_2, and reached the highest value in the CMC-PP-SH (35.0 %, 39.1 %, 47.0 %, and 55.3 wt%, respectively). The temperature at which 10 % weight loss occurs during the thermal degradation process (T_{d10}) values obtained for the pristine CMC, CMC-PP, CMC-PP-NH_2, and CMC-PP-SH nanocomposites were 299.5 °C, 241.6 °C, 267.4 °C, and 350.5 °C, respectively. A higher T_{d10} value suggests that the material can withstand higher temperatures before significant degradation occurs. CMC-PP-SH nanocomposite exhibited much higher thermal stability than the other samples. Conversely, the pristine CMC and the CMC-PP nanocomposite has the lowest thermal stability.

3.5. Morphology

The SEM analysis of CMC-PP, CMC-PP-APTS, and CMC-PP-MPTS shows that they have coarse and porous morphologies (Fig. 4a-c). The SEM micrographs indicate that the CMC-PP has maintained its morphology after surface modifications with different silanes. Additionally, TEM analysis revealed that the composite particles consist of tiny aggregates with different particle sizes based on the specific modification (Fig. 4d-f).

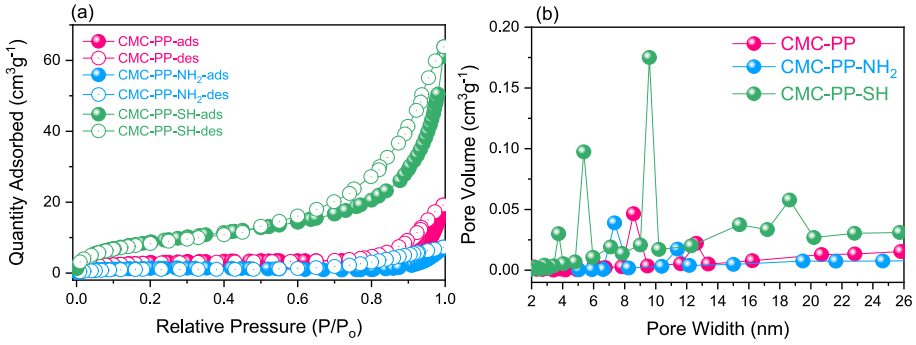

Fig. 3. BET isotherms (a) and pore size distributions (b) of CMC-PP, CMC-PP-NH_2, and CMC-PP-SH nanocomposites.

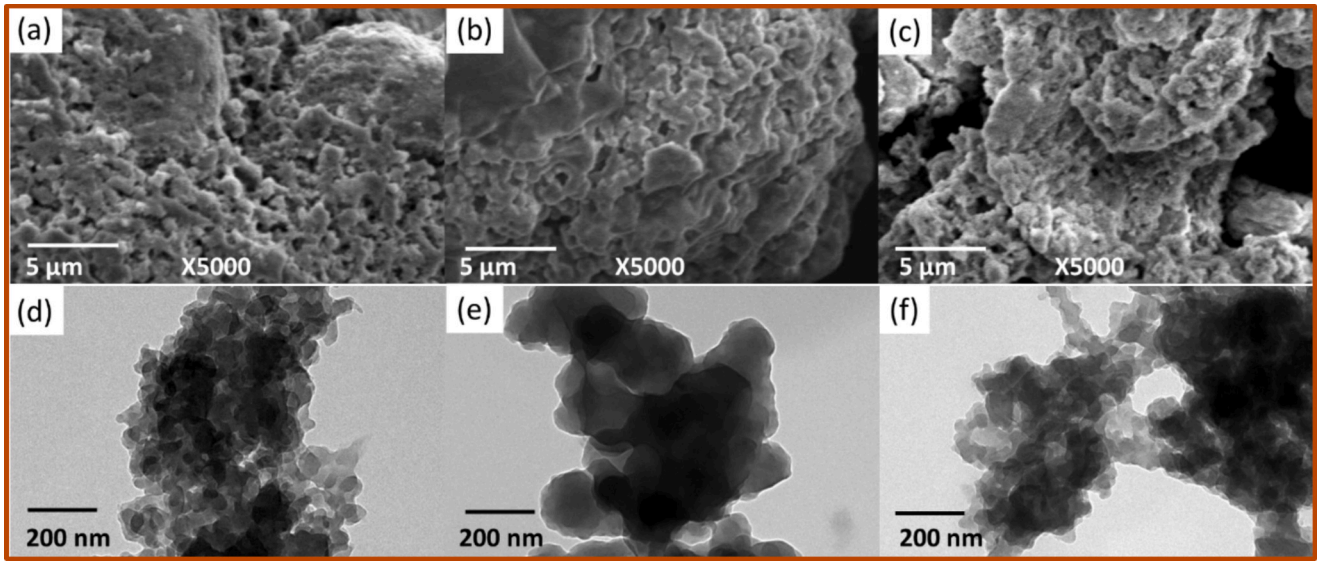

Fig. 4. SEM micrographs of CMC-PP (a), CMC-PP-NH_2 (b) and CMC-PP-SH (c) nanocomposites, and TEM images of CMC-PP (d), CMC-PP-NH_2 (e) and CMC-PP-SH (f) nanocomposites.

3.6. Gas uptakes

The CMC-PP nanocomposites were tested for gas capture. Fig. 5 demonstrates that CMC-PP composite has CO_2 maximum adsorption capacities of 7.42 cm^3g^{-1} at 273 K and 5.47 cm^3g^{-1} at 298 K, while pristine CMC shows a CO_2 capture of only 3.47 and 2.57 cm^3g^{-1} at 273 and 268 K respectively (Fig. S4). The notable increase in adsorption capacities indicates that the CMC-PP nanocomposite is a promising candidate for capturing CO_2. The higher adsorption capacity observed at lower temperatures (273 K) is consistent with the behaviour of many adsorbents, where gas adsorption typically increases as temperature decreases (Gao et al., 2020; Kotp, El-Mahdy, et al., 2024). This phenomenon occurs because lower temperatures reduce the kinetic energy of gas molecules, allowing for greater interaction with the adsorbent material (Moein & Logeswaran, 2014). Despite the relatively low BET surface area of 10.35 m^2g^{-1} compared to other advanced materials used for CO_2 capture, such as activated carbons or metal-organic frameworks (MOFs) (Hu et al., 2019), the unique combination of CMC and PP may provide additional functionality. The derivation of the CMC-PP-NH_2 nanocomposite significantly alters the material's properties, particularly in terms of surface area and CO_2 capture capabilities. While the CMC-PP-NH_2 nanocomposite exhibits a decreased surface area of 4.49 m^2g^{-1} compared to the CMC-PP nanocomposite, it demonstrates a remarkable increase in CO_2 adsorption, with capacities of 25.97 cm^3g^{-1} at 273 K and 12.98 cm^3g^{-1} at 298 K (Fig. 5a-b). This enhancement in gas capture performance underscores the impact of surface functionalization on the adsorption properties of nanocomposite materials. The coating of CMC-PP with APTS introduces amino groups to the surface of the

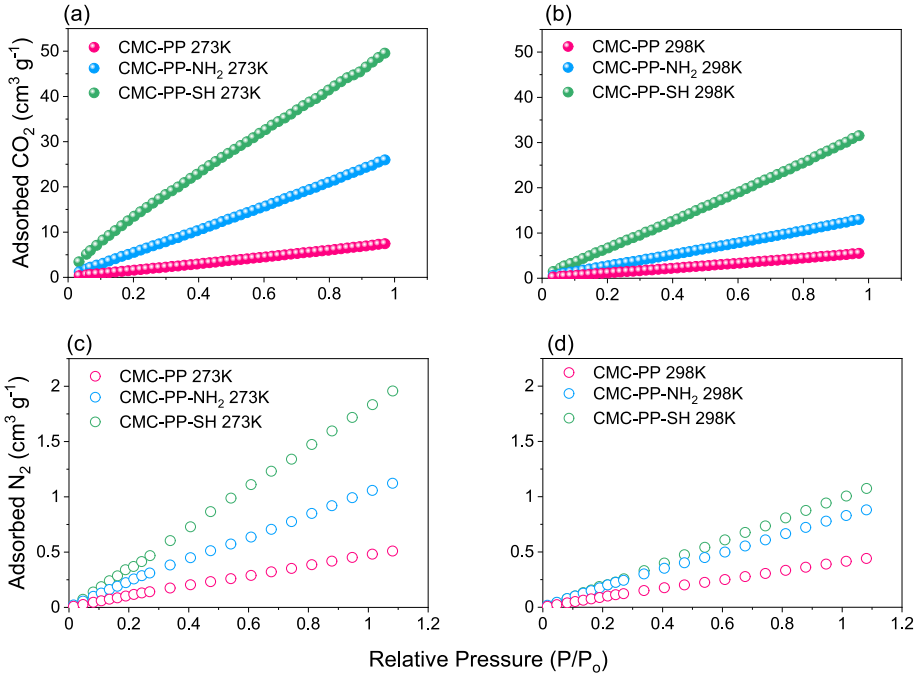

Fig. 5. The capture isotherm of CO_2 (a, b) and N_2 (c, d) at 273 K and 298 K utilizing CMC-PP, CMC-PP-NH_2, and CMC-PP-SH nanocomposites.

nanocomposite. The amino groups are essential in strengthening and facilitating reversible interactions with CO_2, which are critical for effective gas capture (Fan & Jia, 2022; Yang et al., 2012).

The formation of the CMC-PP-SH nanocomposite was accompanied by a significant increase in the material's surface area and enhanced porosity compared to the CMC-PP nanocomposite. In the same manner, the CMC-PP-SH nanocomposite exhibits enhanced CO_2 capture capabilities, achieving adsorption capacities of 49.55 cm^3g^{-1} at 273 K and 31.49 cm^3g^{-1} at 298 K (Fig. 5a-b). These results indicate that the incorporation of mercapto-silane not only improves the structural properties of the nanocomposite but also enhances its functionality for gas capture applications. The mercapto-functional groups within the CMC-PP-SH nanocomposite can create additional active sites for gas adsorption, facilitating the interaction with CO_2 molecules (Ma et al., 2022). The enhanced surface area provides more opportunities for CO_2 to interact with the nanocomposite, (Niu et al., 2016). The thiol groups can interact with CO_2 through various mechanisms, including hydrogen bonding and potential chemisorption, which enhances the overall affinity of the material for CO_2 (Saha & Kienbaum, 2019). Moreover, the presence of mesopores (2–50 nm) is particularly beneficial for gas adsorption, as they facilitate the diffusion of gas molecules into the material and provide adequate space for adsorption. Furthermore, the CMC-PP-SH nanocomposite exhibits a broader range of pore sizes compared to CMC-PP-NH_2, which may enhance its ability to capture CO_2 effectively. The smaller pores in CMC-PP-SH can provide more surface interactions with CO_2 molecules, while larger pores can facilitate gas diffusion.

The measured N_2 uptakes of the CMC-PP, CMC-PP-NH_2, and CMC-PP-SH nanocomposites at different temperatures are presented in Fig. 5c,d. The results indicate a clear trend of increasing N_2 adsorption capacity from CMC-PP to CMC-PP-NH_2 and further to CMC-PP-SH nanocomposites. The CMC-PP nanocomposite exhibits the lowest N_2 uptake among the three materials, with values of 0.50 $cm^3\ g^{-1}$ at 273 K and 0.44 cm^3g^{-1} at 298 K. The introduction of amino ($-NH_2$) groups through the CMC-PP-NH_2 nanocomposite has enhanced the uptake of N_2 molecules. The N_2 adsorption capacities for CMC-PP-NH_2 are 1.12 $cm^3\ g^{-1}$ at 273 K and 0.88 $cm^3\ g^{-1}$ at 298 K. The CMC-PP-SH nanocomposite exhibits the highest N_2 uptake among the three materials, with capacities of 1.95 $cm^3\ g^{-1}$ at 273 K and 1.07 $cm^3\ g^{-1}$ at 298 K. The introduction of thiol (-SH) groups through the MPTS coating enhances the interactions between the nanocomposite surface and N_2 molecules.

The selectivity data obtained using Henry's model constant, based on the slopes of the gas uptake isotherms at lower pressures (up to 0.16 bar), further supports the effectiveness of these nanocomposites for CO_2/N_2 separation. The selectivity values indicate the ability of each nanocomposite to preferentially adsorb CO_2 over N_2. At 273 K, the CO_2/N_2 selectivity values for the nanocomposites are 14.57 for CMC-PP, 23.15 for CMC-PP-NH_2, and 25.32 for CMC-PP-SH (Fig. 6). The observed trend shows that the selectivity increases significantly with the introduction of functional groups.

The CMC-PP-SH nanocomposite exhibits the highest selectivity, reaching 25.32 at 273 K (Table S2). The thiol groups can facilitate both physisorption and chemisorption mechanisms, leading to a more effective capture of CO_2. CMC-PP, CMC-PP-NH_2, and CMC-PP-SH nanocomposite show higher CO_2 adsorption capacities than earlier reported materials (Table S3).

3.7. Isotherms studies

The standard enthalpy changes (isosteric heat of sorption, Q_{st}) for CO_2 capture by the CMC-PP, CMC-PP-NH_2, and CMC-PP-SH nanocomposites, calculated using the Clausius-Clapeyron equation, provide valuable insights into the energetics of the adsorption process (Fig. 7). The Q_{st} values indicate the amount of energy released or absorbed during the adsorption of CO_2 onto the nanocomposite surfaces. At a pressure of 0.15 bar, the Q_{st} values are 8.94 kJ/mol for CMC-PP, 20.41 kJ/mol for CMC-PP-NH_2, and 30.86 kJ/mol for CMC-PP-SH. At a higher pressure of 0.25 bar, the Q_{st} values are 7.86 kJ/mol for CMC-PP, 20.8 kJ/mol for CMC-PP-NH_2, and 26 kJ/mol for CMC-PP-SH (Fig. 7a). These results demonstrate that the introduction of functional groups, particularly amino (-NH_2) and thiol (-SH) groups, significantly enhances the heat of adsorption for CO_2 capture. CMC-PP-SH nanocomposite exhibits the highest Q_{st} among the three materials. The thiol groups provide stronger interactions with CO_2 than amino groups, facilitating both

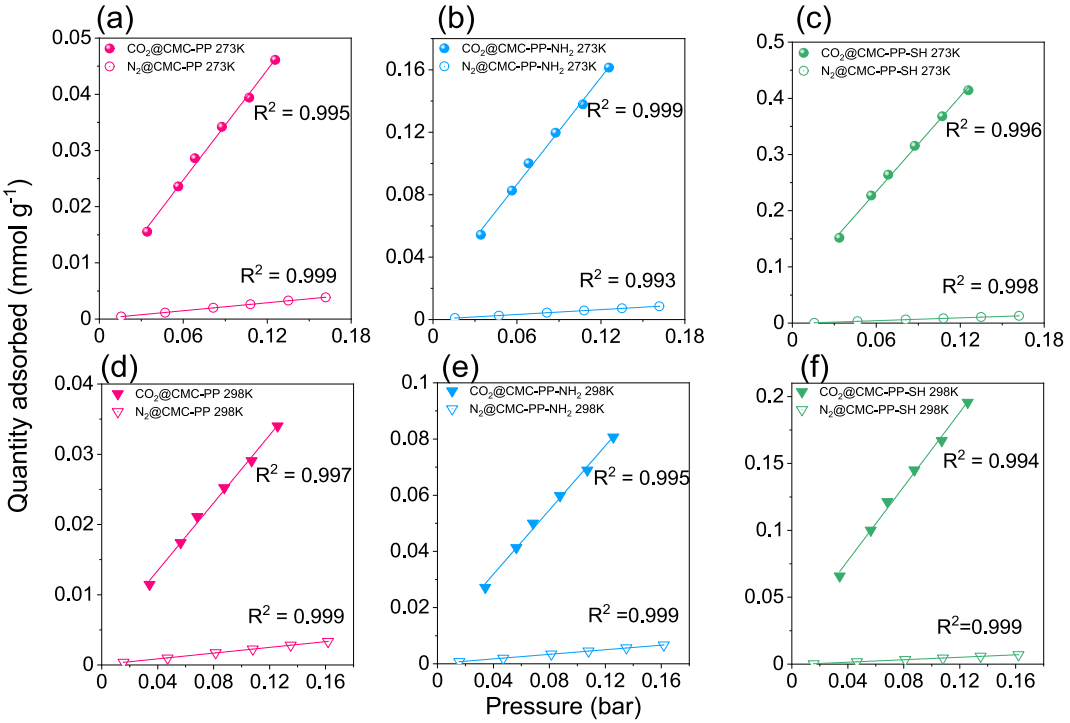

Fig. 6. Selective gas capture at 273 K (a-c) and 298 K (d-f) of those CMC-PP, CMC-PP-NH_2, and CMC-PP-SH nanocomposites respectively utilizing Henry's model.

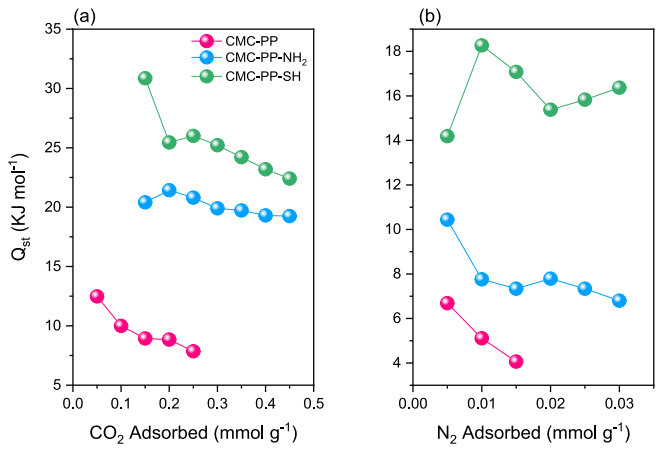

Fig. 7. Isosteric heats of CO_2 (a) and N_2 (b) uptakes utilizing CMC-PP, CMC-PP-NH_2, and CMC-PP-SH nanocomposites.

physisorption and chemisorption mechanisms.

The decrease in Q_{st} values with increasing pressure from 0.15 bar to 0.25 bar is typical behaviour of adsorbents (Rahmani et al., 2023). As pressure increases, the adsorption capacity also increases, but the additional adsorption sites may not be as energetically favourable as the initial sites, resulting in lower heat of adsorption (Li et al., 2019). Q_{st} for N_2 capture by the CMC-PP, CMC-PP-NH_2, and CMC-PP-SH nanocomposites (Fig. 7b), show a similar behaviour of CO_2 uptake. At a pressure of 0.005 bar, the Q_{st} values were found to be 6.69 kJ/mol for CMC-PP, 10.44 kJ/mol for CMC-PP-NH_2, and 14.19 kJ/mol for CMC-PP-SH. At a higher pressure of 0.015 bar, the Q_{st} values were found to be 4.06 kJ/mol for CMC-PP, 7.37 kJ/mol for CMC-PP-NH_2, and 17.08 kJ/mol for CMC-PP-SH. The CMC-PP nanocomposite low Q_{st} value indicates that the energy released during the adsorption process is minimal, reflecting the limited capacity of the CMC-PP nanocomposite to effectively capture N_2. In contrast, the CMC-PP-NH_2 nanocomposite exhibits a notable increase in Q_{st} values due to the enhanced interactions with N_2 through hydrogen bonding and other reversible interactions. The CMC-PP-SH nanocomposite exhibits the highest Q_{st} values among the three materials due to stronger interactions with N_2. As pressure increases, the Q_{st} decreases, aligning with previous results regarding the CO_2 uptake and selectivity of nanocomposites.

The observed values of N_2 adsorption and corresponding Q_{st} at different points in the CMC-PP-SH track, indicate that at the initial stage, fewer N_2 molecules are interacting with the surface of CMC-PP-SH, resulting in weaker overall interactions. The limited number of occupied active sites means that the energy associated with these interactions is not maximized. As we move to the next point (0.01 $mmolg^{-1}$), where more nitrogen is adsorbed, Q_{st} is increased to 18.27 kJ/mol. This increase reflects stronger interactions occurring as more active sites become occupied, particularly those with higher binding energy, and leads to enhance overall adsorption energy. After reaching the second point, the trend reverses with subsequent measurements showing lower Q_{st} values (15.83 kJ/mol at 0.025 $mmolg^{-1}$ and 15.38 kJ/mol at 0.02 $mmolg^{-1}$). This decrease implies the saturation of high-energy sites on the adsorbent surface.

3.8. Recycling efficacy

The recycling tests for CO_2 capture using CMC-PP-NH_2 and CMC-PP-SH nanocomposites reveal that the latter significantly outperforms the former at both 273 K and 298 K, with average capacities of 47.466 cm^3g^{-1} and 31.145 cm^3g^{-1}, compared to 24.210 $cm^3\ g^{-1}$ and 11.633 cm^3g^{-1}, respectively (Fig. S5). Notably, the thiol groups in CMC-PP-SH more favourably facilitate the interactions for CO_2 capture than the amine groups in CMC-PP-NH_2. In addition, CMC-PP-SH exhibits better stability and effectiveness over multiple recycling cycles. In other words, at 273 K, the CMC-PP-NH_2 maintained over 95.7 % adsorption capacity throughout five cycles (Fig. S5), and CMC-PP-SH exhibited consistent performance (96.8 %). Similarly, at 298 K, both nanocomposites showed strong retention of CO_2 adsorption capacity, with CMC-PP-NH_2 reaching up to 98.7 % in the second cycle, then declined to 84.2 % in the fifth cycle. These results underscore the high performance and reliability of these nanocomposites for practical applications in gas separation and capture.

3.9. Gas uptake mechanism

The fitting of adsorption isotherms for CO_2 and N_2 capture using the Langmuir (eq. 1,2 and Fig. S6), DSL (eq. 3,4 and Fig. 8), and Sips (eq. 5,2 and Fig. S7) models on the CMC-PP, CMC-PP-NH_2, and CMC-PP-SH nanocomposites provides critical insights into the adsorption mechanisms and efficiencies of these materials (the parameters of the eq1–5 are defined in the supporting information file) (Wang et al., 2020). The results indicate that the DSL model provides the best fit for CO_2 adsorption, with a correlation coefficient exceeding 0.999. This suggests that the adsorption of CO_2 takes place over multiple adsorption sites with varied affinities, which is due to the different functional groups.

$$q_0 = \frac{q_m + bp}{1 + bp} \tag{1}$$

$$b = b_0 exp\left(\frac{\Delta H}{RT}\right) \tag{2}$$

$$q = \frac{q_1 b_1 p}{1 + b_1 p} + \frac{q_2 b_2 p}{1 + b_2 p} \tag{3}$$

$$b_i = b_{i0}\ exp\left(\frac{\Delta H_i}{RT}\right) \tag{4}$$

$$q = \frac{q_m (bp)^{1/n}}{1 + (bp)^{1/n}} \tag{5}$$

The DSL model's superior fit implies that the CMC-PP, CMC-PP-NH_2, and CMC-PP-SH nanocomposites have heterogeneous surfaces (Table S4), where different sites exhibit distinct adsorption energies. This heterogeneity is particularly relevant for CO_2 capture, as the functionalization of the nanocomposites with amino and thiol groups creates a varied landscape for gas interactions (Sharma et al., 2018). The presence of these functional groups likely leads to stronger interactions with CO_2, facilitating its adsorption compared to N_2, which may interact primarily through weaker physical adsorption mechanisms. Importantly, the alignment of CO_2 adsorption behaviour with the DSL model for CMC-PP, CMC-PP-NH_2, and CMC-PP-SH nanocomposites indicates their heterogeneous surfaces with diverse adsorption sites, enhancing CO_2 capture efficiency through distinct interaction mechanisms and selectivity over N_2. The observed trends in the isotherm fitting are consistent with the above-discussed results regarding the selectivity and Q_{st} for both gases. Once again, in the context of the DSL model, Q_{st} can be derived from the adsorption isotherms obtained at various loadings and allows calculating Q_{st} by analysing how adsorption energy changes with varying CO_2 loadings. Specifically, as CO_2 fills various types of sites on the nanocomposite, Q_{st} changes depending on whether CO_2 is interacting with high-energy or low-energy sites. The differences in adsorption behaviour between CO_2 and N_2 is attributed to the functional groups present in the nanocomposites.

Interestingly, the mechanism of CO_2 adsorption on functionalized CMC-PP-NH_2 and CMC-PP-SH, involves both physisorption and chemisorption processes. Both amino and thiol groups can participate in physisorption; however, thiol groups are particularly effective due to their ability to create a more polar environment that enhances

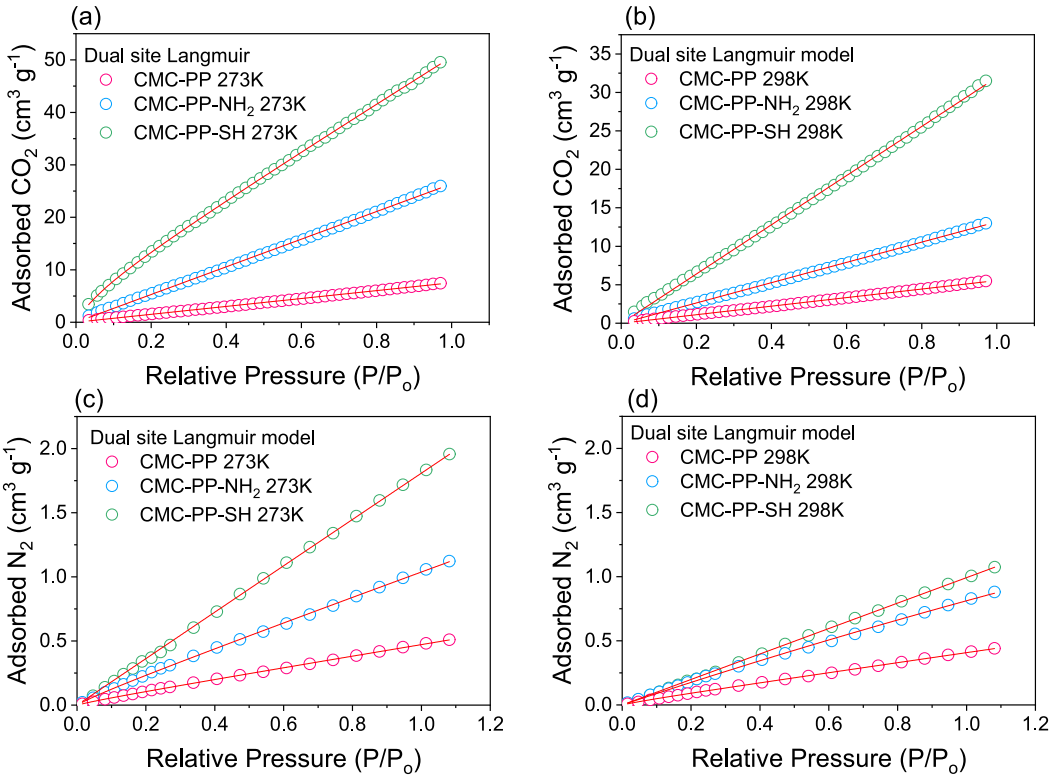

Fig. 8. The fitting isotherm of CO_2 capture using the Dual site Langmuir isotherm (a, b) and N_2 (c, d) at 273 K and 298 K with CMC-PP, CMC-PP-NH_2, and CMC-PP-SH nanocomposites.

interaction with CO_2. This involves weak van der Waals forces and hydrogen bonding between CO_2 molecules and the surface of the nanocomposites. On the other hand, chemisorption involves the formation of stronger chemical bonds between CO_2 and the functional groups on the adsorbent surface. The amino groups can react with CO_2 to form carbamate species, which enhances CO_2 capture, while the thiol groups can facilitate stronger interactions by forming thiocarbamate or other sulfur-containing complexes with CO_2 (Forse & Milner, 2021; Mannisto et al., 2021).

4. Conclusions

This study demonstrates the remarkable effectiveness of CMC-PP nanocomposites in capturing CO_2, confirming our hypothesis that the incorporation of PP can significantly enhance the CO_2 adsorption capacity through synergistic interactions. The introduction of amino and thiol groups via coatings with APTS and MPTS has proven to be pivotal, with the CMC-PP-SH nanocomposite achieving a CO_2 adsorption capacity of 49.55 cm^3g^{-1} at 273 K. This enhancement is attributed to the favourable adsorption kinetics and selectivity exhibited by the thiol-functionalized nanocomposite. The dual-site Langmuir model fitting indicates a heterogeneous adsorption process, while the calculated standard Q_{st} confirms the energetic advantages provided by thiol functionalization. These findings underscore the potential of SH-silane coatings in developing advanced materials for effective gas separation applications. Our research highlights the role of carbohydrate polymers like CMC in creating innovative solutions for sustainable CO_2 capture technologies. By demonstrating that PP can facilitate sol-gel interactions, we present a streamlined approach to synthesizing these nanocomposites, enhancing their practical applicability in environmental remediation efforts. Furthermore, our results contribute to the growing body of literature on biopolymer-based materials and their critical role in addressing climate change through effective carbon capture strategies.

CRediT authorship contribution statement

Mohammed G. Kotp: Writing – review & editing, Writing – original draft, Visualization, Investigation, Data curation, Formal analysis, Conceptulatization. **Islam M. Minisy:** Writing – review & editing, Formal analysis, Conceptualization. **Basel Al-Saida:** Formal analysis, Data curation. **Shiao-Wei Kuo:** Writing – review & editing, Supervision, Resources, Funding acquisition.

Declaration of competing interest

The authors declare that they have no known competing financial interests or personal relationships that could have appeared to influence the work reported in this paper.

Acknowledgments

This study was supported financially by the National Science and Technology Council, Taiwan, under contracts NSTC 113-2223-E-110-001 and 113-2218-E-110-004. The authors thank the staff at National Sun Yat-sen University for their assistance with the TEM (ID: EM022600) experiments.

Appendix A. Supplementary data

Supplementary data to this article can be found online at https://doi.org/10.1016/j.carbpol.2025.123399.

Data availability

Data will be made available on request.

References

Adhikari, A., De, S., Halder, A., Pattanayak, S., Dutta, K., Mondal, D., … Chattopadhyay, S. (2018). Biosurfactant tailored synthesis of porous polypyrrole nanostructures: A facile approach towards CO2 adsorption and dopamine sensing. *Synthetic Metals, 245*, 209–222.

Ahmed, M., Kotp, M. G., Mansoure, T. H., Lee, R.-H., Kuo, S.-W., & EL-Mahdy, A. F. M. (2022). Ultrastable carbazole-tethered conjugated microporous polymers for high-performance energy storage. *Microporous and Mesoporous Materials, 333*, Article 111766. https://doi.org/10.1016/j.micromeso.2022.111766

Banerjee, P., Chowdhury, M., Das, P., Nadda, A. K., & Mukhopadhayay, A. (2023). *"Biopolymers for CO2 capture", CO2-philic polymers* (pp. 289–320). Nanocomposites and Chemical Solvents: Elsevier.

Barsoum, M. L., Hofmann, J., Xie, H., Chen, Z., Vornholt, S. M., Dos Reis, R., … Dravid, V. P. (2024). Probing structural transformations and degradation mechanisms by direct observation in SIFSIX-3-Ni for direct air capture. *Journal of the American Chemical Society, 146*, 6557–6565.

Boubaker, S., Liu, Z., Mu, Y., & Zhan, Y. (2024). *Carbon dioxide emissions and environmental risks: Long term and short term.* Risk Analysis.

Chao, C., Deng, Y., Dewil, R., Baeyens, J., & Fan, X. (2021). Post-combustion carbon capture. *Renewable and Sustainable Energy Reviews, 138*, Article 110490.

Chen, M., Gu, Q., Shao, H., Liu, H., Luan, J., Yan, Z., … Ke, X. (2023). How PPY/CMC aerogels possess selective adsorption capacity for norfloxacin: Coupling molecular scale interpretation with experiments. *Chemical Engineering Journal, 464*, Article 142485.

Deng, Q.-F., Liu, L., Lin, X.-Z., Du, G., Liu, Y., & Yuan, Z.-Y. (2012). Synthesis and CO2 capture properties of mesoporous carbon nitride materials. *Chemical Engineering Journal, 203*, 63–70.

Fan, Y., & Jia, X. (2022). Progress in amine-functionalized silica for CO2 capture: Important roles of support and amine structure. *Energy & Fuels, 36*, 1252–1270.

Fatima, S. S., Borhan, A., Ayoub, M., & Abd Ghani, N. (2021). Development and progress of functionalized silica-based adsorbents for CO2 capture. *Journal of Molecular Liquids, 338*, Article 116913.

Forse, A. C., & Milner, P. J. (2021). New chemistry for enhanced carbon capture: Beyond ammonium carbamates. *Chemical Science, 12*, 508–516.

Gao, Z., Li, B., Li, J., Zhang, Y., Ren, C., & Wang, B. (2020). Study on the adsorption and thermodynamic characteristics of methane under high temperature and pressure. *Energy & Fuels, 34*, 15878–15893.

Habibi, N. (2014). Preparation of biocompatible magnetite-carboxymethyl cellulose nanocomposite: Characterization of nanocomposite by FTIR, XRD, FESEM and TEM. *Spectrochimica Acta. Part A, Molecular and Biomolecular Spectroscopy, 131*, 55–58.

Hsiao, C.-W., Elewa, A. M., Mohamed, M. G., Kotp, M. G., Chou, M. M.-C., & Kuo, S.-W. (2024). *Designing strategically functionalized hybrid porous polymers with Octavinylsilsesquioxane/Dibenzo [g, p] chrysene/benzo [c]-1, 2, 5-thiadiazole units for rapid removal of rhodamine B dye from water* (p. 134658). A Physicochem. Eng. Asp: Colloids Surf.

Hu, Z., Wang, Y., Shah, B. B., & Zhao, D. (2019). CO2 capture in metal–organic framework adsorbents: An engineering perspective. *Advanced Sustainable Systems, 3*, 1800080.

Kawasaki, T., Nakaji-Hirabayashi, T., Masuyama, K., Fujita, S., & Kitano, H. (2016). Complex film of chitosan and carboxymethyl cellulose nanofibers. *Colloids and Surfaces. B, Biointerfaces, 139*, 95–99.

Kotp, M. G., Elewa, A. M., EL-Mahdy, A. F. M., Chou, H.-H., & Kuo, S.-W. (2021). Tunable Pyridyl-based conjugated microporous polymers for visible light-driven hydrogen evolution. *ACS Applied Energy Materials, 4*, 13140–13151. https://doi.org/10.1021/acsaem.1c02772

Kotp, M. G., El-Mahdy, A. F. M., Chou, M. M., & Kuo, S.-W. (2024). Electronic nature of linkers based conjugated microporous polymers: A sustainable approach to enhance CO2 capture. *New Journal of Chemistry, 48*, 14435–14443.

Kotp, M. G., & Kuo, S.-W. (2024). Selective capturing of the CO2 emissions utilizing ecological (3-mercaptopropyl)trimethoxysilane-coated porous organic polymers in composite materials. *Polymers, 13*, 1759. https://doi.org/10.3390/polym16131759

Kotp, M. G., Kuo, S.-W., & EL-Mahdy, A. F. M. (2024). *Phenazine-based conjugated microporous polymers: Influence of planarity and imine content on energy storage performance* (p. 133210). A Physicochem. Eng. Asp: Colloids Surf.

Kotp, M. G., Torad, N. L., Lüder, J., El-Amir, A., Chaikittisilp, W., Yamauchi, Y., & EL-Mahdy, A. F. M. (2023). A phenazine conjugated microporous polymer-based quartz crystal microbalance for sensitive detection of formaldehyde vapors at room temperature: An experiment and density functional theory study. *Journal of Materials Chemistry A, 11*, 764–774. https://doi.org/10.1039/D2TA07966F

Kotp, M. G., Torad, N. L., Nara, H., Chaikittisilp, W., You, J., Yamauchi, Y., … Kuo, S.-W. (2023). Tunable Thiophene-based conjugated microporous polymers for the disposal of toxic hexavalent chromium. *Journal of Materials Chemistry A, 11*, 15022–15032.

Kumar, A., Prasad, S., Saxena, P. N., Ansari, N. G., & Patel, D. K. (2021). Synthesis of an alginate-based Fe3O4–MnO2 xerogel and its application for the concurrent elimination of Cr (VI) and cd (II) from aqueous solution. *ACS Omega, 6*, 3931–3945.

Kumar, N., Rajendran, H. K., Ray, J., & Narayanasamy, S. (2022). Sequestration and toxicological assessment of emerging contaminants with polypyrrole modified carboxymethyl cellulose (CMC/PPY): Case of ibuprofen pharmaceutical drug. *International Journal of Biological Macromolecules, 221*, 547–557.

Li, J., Wu, K., Chen, Z., Wang, W., Yang, B., Wang, K., … Yu, R. (2019). Effects of energetic heterogeneity on gas adsorption and gas storage in geologic shale systems. *Applied Energy, 251*, Article 113368.

Ma, J., Li, Y., Li, J., Yang, X., Ren, Y., Alghamdi, A. A., … Deng, Y. (2022). Rationally designed dual-mesoporous transition metal oxides/Noble metal nanocomposites for fabrication of gas sensors in real-time detection of 3-Hydroxy-2-butanone biomarker. *Advanced Functional Materials, 32*, 2107439.

Mannisto, J. K., Pavlovic, L., Tiainen, T., Nieger, M., Sahari, A., Hopmann, K. H., & Repo, T. (2021). Mechanistic insights into carbamate formation from CO 2 and amines: The role of guanidine–CO 2 adducts. *Catalysis Science & Technology, 11*, 6877–6886.

Minisy, I. M., Acharya, U., Veigel, S., Morávková, Z., Taboubi, O., Hodan, J., … Bober, P. (2021). Sponge-like polypyrrole–nanofibrillated cellulose aerogels: Synthesis and application. *Journal of Materials Chemistry C, 9*, 12615–12623.

Minisy, I. M., Gupta, S., Taboubi, O., Acharya, U., & Bober, P. (2024). Polypyrrole/tungsten carbide nanocomposites for electrochemical applications. *ACS Applied Polymer Materials, 6*, 8244–8253.

Moein, S., & Logeswaran, R. (2014). KGMO: A swarm optimization algorithm based on the kinetic energy of gas molecules. *Information Sciences, 275*, 127–144.

Mohamed, M. G., EL-Mahdy, A. F. M., Kotp, M. G., & Kuo, S.-W. (2022). Advances in porous organic polymers: Syntheses, structures, and diverse applications. *Materials Advances, 3*, 707–733. https://doi.org/10.1039/D1MA00771H

Mousa, A. O., Mohamed, M. G., Chuang, C.-H., & Kuo, S.-W. (2023). Carbonized aminal-linked porous organic polymers containing pyrene and triazine units for gas uptake and energy storage. *Polymers, 15*, 1891.

Mudassir, M. A., Aslam, H. Z., Ansari, T. M., Zhang, H., & Hussain, I. (2021). Fundamentals and design-led synthesis of emulsion-templated porous materials for environmental applications. *Advancement of Science, 8*, 2102540.

Niu, M., Yang, H., Zhang, X., Wang, Y., & Tang, A. (2016). Amine-impregnated mesoporous silica nanotube as an emerging nanocomposite for CO2 capture. *ACS Applied Materials & Interfaces, 8*, 17312–17320.

Ouyang, J., Gu, W., Zheng, C., Yang, H., Zhang, X., Jin, Y., … Jiang, J. (2018). Polyethyleneimine (PEI) loaded MgO-SiO2 nanofibers from sepiolite minerals for reusable CO2 capture/release applications. *Applied Clay Science, 152*, 267–275.

Prodan, D., Moldovan, M., Furtos, G., Saroși, C., Filip, M., Perhaița, I., Carpa, R., Popa, M., Cuc, S., & Varvara, S. (2021). Synthesis and characterization of some graphene oxide powders used as additives in hydraulic mortars. *Applied Sciences, 11*, 11330.

Qiu, K., & Netravali, A. N. (2014). A review of fabrication and applications of bacterial cellulose based nanocomposites. *Polymer Reviews, 54*, 598–626.

Rahman, M. S., Hasan, M. S., Nitai, A. S., Nam, S., Karmakar, A. K., Ahsan, M. S., … Ahmed, M. B. (2021). *Recent developments of carboxymethyl cellulose. Polymers., 13*, 1345.

Rahmani, M., Mokhtarani, B., & Rahmanian, N. (2023). High pressure adsorption of hydrogen sulfide and regeneration ability of ultra-stable Y zeolite for natural gas sweetening. *Fuel, 343*, Article 127937.

Rapheal, G., Kumar, S., Scharnagl, N., & Blawert, C. (2016). Effect of current density on the microstructure and corrosion properties of plasma electrolytic oxidation (PEO) coatings on AM50 mg alloy produced in an electrolyte containing clay additives. *Surface and Coating Technology, 289*, 150–164.

Saha, D., & Kienbaum, M. J. (2019). Role of oxygen, nitrogen and sulfur functionalities on the surface of nanoporous carbons in CO2 adsorption: A critical review. *Microporous and Mesoporous Materials, 287*, 29–55.

Seidi, F., Arabi Shamsabadi, A., Ebadi Amooghin, A., Saeb, M. R., Xiao, H., Jin, Y., & Rezakazemi, M. (2022). Biopolymer-based membranes from polysaccharides for CO2 separation: A review. *Environmental Chemistry Letters, 20*, 1083–1128.

Sharma, P., Chakrabarty, S., Roy, S., & Kumar, R. (2018). Molecular view of CO2 capture by polyethylenimine: Role of structural and dynamical heterogeneity. *Langmuir, 34*, 5138–5148.

Shishatskiy, S., Pauls, J. R., Nunes, S. P., & Peinemann, K.-V. (2010). Quaternary ammonium membrane materials for CO2 separation. *Journal of Membrane Science, 359*, 44–53.

Tanzifi, M., Yaraki, M. T., Beiramzadeh, Z., Saremi, L. H., Najafifard, M., Moradi, H., … Bazgir, H. (2020). Carboxymethyl cellulose improved adsorption capacity of polypyrrole/CMC composite nanoparticles for removal of reactive dyes: Experimental optimization and DFT calculation. *Chemosphere, 255*, Article 127052.

Venturi, D., Chrysanthou, A., Dhuiège, B., Missoum, K., & Giacinti Baschetti, M. (2019). Arginine/Nanocellulose membranes for carbon capture applications. *Nanomaterials, 9*, 877.

Wang, Z., Goyal, N., Liu, L., Tsang, D. C., Shang, J., Liu, W., & Li, G. (2020). N-doped porous carbon derived from polypyrrole for CO2 capture from humid flue gases. *Chemical Engineering Journal, 396*, Article 125376.

Wu, D., Zhang, Y., Huang, J., Zhao, X., Peng, B., Liu, W., & Feng, Y. (2024). Cellulose-based irreversible hydrogels used for CO2 sequestration. *ACS Sustain. Chem. Eng. ACS., 12*, 7950–7963.

Yang, M., & Wang, Y. (2024). D-BJH: The intrinsic model for characterizing the pore size distribution of porous materials. *Langmuir, 40*, 20368–20378.

Yang, Z.-Z., He, L.-N., Gao, J., Liu, A.-H., & Yu, B. (2012). Carbon dioxide utilization with C–N bond formation: carbon dioxide capture and subsequent conversion. *Energy & Environmental Science, 5*, 6602–6639.